JOURNAL OF AIRCRAFT
Vol. 43, No. 3, May–June 2006

Rotor Airloads Prediction Using Loose Aerodynamic/Structural Coupling

Mark Potsdam,* Hyeonsoo Yeo,† and Wayne Johnson†
NASA Ames Research Center, Moffett Field, California 94035

A computational fluid dynamics (CFD) code and rotorcraft computational structural dynamics (CSD) code are coupled to calculate helicopter rotor airloads across a range of flight conditions. An iterative loose (weak) coupling methodology is used to couple the CFD and CSD codes on a per revolution, periodic basis. The CFD code uses a high fidelity, Navier–Stokes, overset grid methodology with first principles-based wake capturing. Modifications are made to the CFD code for the aeroelastic analysis. For a UH-60A Blackhawk helicopter, three challenging level flight conditions are computed: 1) high speed, $\mu = 0.37$, with advancing blade negative lift, 2) low speed, $\mu = 0.15$, with blade–vortex interaction, and 3) high thrust with dynamic stall, $\mu = 0.24$. Results are compared with UH-60A Airloads Program flight test data. For all cases the loose coupling methodology is shown to be stable, convergent, and robust with full coupling of normal force, pitching moment, and chord force. In comparison with flight test data, normal force and pitching moment phase and magnitude are in good agreement. The shapes of the airloads curves are well captured. Overall, the results are a noteworthy improvement over lifting line aerodynamics used in rotorcraft comprehensive codes.

Nomenclature

a = speed of sound
C_T = thrust coefficient
c = blade chord
M = section pitching moment per unit length
M_{tip} = hover tip Mach number
M_∞ = freestream Mach number
M^2c_m = section pitching moment coefficient, $M/\frac{1}{2}\rho a^2 c^2$
M^2c_n = section normal force coefficient, $N/\frac{1}{2}\rho a^2 c$
N = section normal force per unit length
R = blade radius
r = radial coordinate
z = rotor shaft coordinate
α_s = shaft angle, deg
β = side-slip angle, +nose left, deg
β_0 = coning angle, deg
β_{1c}, β_{1s} = flapping, longitudinal and lateral, deg
θ_0 = collective angle, deg
θ_{1c}, θ_{1s} = cyclic, lateral and longitudinal, deg
μ = advance ratio, M_∞/M_{tip}
ρ = air density
σ = rotor solidity
ψ = rotor azimuth angle, 0 aft, deg

Introduction

ANALYSIS of helicopter rotors is a challenging multidisciplinary problem. Successful aerodynamic analysis of this problem requires accurate capabilities for modeling unsteady, three-dimensional flowfields, transonic flow with shocks, reversed flow, dynamic stall, vortical wakes, rigid-body motion, and deformation. This must be combined with a finite element computational structural dynamics (CSD) analysis. In the fully coupled aeroelastic problem, the aerodynamics and structural dynamics interact and are mutually dependent due to rigid and elastic blade motion, airloads, and rotor trim. To handle the overwhelming complexity of the problem, rotorcraft comprehensive codes use lower-order aerodynamics models based on lifting line theory and two-dimensional airfoil tables. Airloads predictions using these fast, low-fidelity aerodynamic methods often show significant shortcomings.

Bousman[1] identified two key unsolved problems in rotor airloads prediction as 1) the azimuthal phase lag of advancing blade negative lift in high-speed flight and 2) the underprediction of blade pitching moments over the entire speed range. The pitching moment magnitude problem extends into dynamic stall where aerodynamic moment prediction is especially important for pitch link loads estimation. These deficiencies in comprehensive code aerodynamics when applied to various helicopter configurations across a range of flight conditions are well documented.[2–4] This was the motivation behind the present work.

The objective of this work is to couple a computational fluid dynamics (CFD) code with a comprehensive rotorcraft analysis to make progress in improving rotorcraft airloads prediction capability. The CFD provides high-fidelity, nonlinear aerodynamics that is expected to overcome the shortcomings in the comprehensive lifting line aerodynamic analysis. It offers a first-principles-based modeling approach for the full flight regime seen on the rotor disk and in the wake. The comprehensive code continues to perform the structural dynamics and trim calculations. Furthermore, an efficient loose coupling approach is taken with the objective of documenting convergence behavior and identifying any shortcomings that might warrant alternative procedures. A range of challenging flight test conditions, high speed with advancing blade negative lift, low speed with blade–vortex interaction, and high thrust with dynamic stall, is used to reach conclusions regarding the appropriateness of the CFD and coupling methodologies. The focus of the work is on airloads prediction: normal force and pitching moment. Performance prediction is not an objective of the current work.

Background

Coupling between CFD and rotorcraft comprehensive codes has been accomplished in two ways. In the loose (weak) coupling methodology, information between CFD and CSD is transferred on a per revolution, periodic basis. In the tight (strong) coupling approach, the CFD and CSD codes are coupled at every time step and integrated simultaneously. Although tight coupling is more rigorous, care must be taken to ensure timewise accuracy between CFD

Received 27 October 2004; revision received 25 February 2005; accepted for publication 28 February 2005. This material is declared a work of the U.S. Government and is not subject to copyright protection in the United States. Copies of this paper may be made for personal or internal use, on condition that the copier pay the $10.00 per-copy fee to the Copyright Clearance Center, Inc., 222 Rosewood Drive, Danvers, MA 01923; include the code 0021-8669/06 $10.00 in correspondence with the CCC.

[*] Aerospace Engineer, US Army Research, Development, and Engineering Command, MS 215-1; mpotsdam@mail.arc.nasa.gov. Senior Member AIAA.

[†] Aerospace Engineer. Member AIAA.

and CSD, and code modification may be required for efficient process communication. Rotor trim for the tight coupling methodology is problematic. On the other hand, loose coupling allows for a modular approach. Each discipline handles its time accuracy as required. Trim is a natural result of the periodic comprehensive analysis.

It remains to be seen if loose coupling has any unexpected drawbacks. An excellent comparison of the two coupling approaches using the CFD codes FLOWer and WAVES and comprehensive code HOST was made by Altmikus et al.[5] A 2.5 times increase in cost for the tight coupling was indicated while yielding very similar solutions for high-speed forward flight conditions. Trim was expediently obtained in a weak coupling fashion. Pomin and Wagner[6] used overset methods and deformable grids in a tight coupling procedure but avoided the trim issue by fixing control angles.

A well-known loose coupling procedure was developed by Tung et al.[7] using a transonic small disturbance (TSD) code. Other TSD[8] and full potential methods[9−11] were later coupled. These CFD methods require inflow angles from the comprehensive code to account for structural deformation, through surface transpiration instead of grid deformation. The inflow angles also include the influence of the wake outside the CFD domain, which is usually limited to the outboard part of the blade and several chords away. Full potential solutions coupled section lift and, with some difficulty, moments, which were shown to have an important effect on torsion prediction. Issues were encountered with convergence[8,10] and complex boundary conditions.[9]

With the continual advancement of high-speed computers, it has become possible to use Euler[5,12] and Navier–Stokes[13−15] CFD in the coupling. Full domain Navier–Stokes analyses do not require the added complexity of inflow angles to model the wake, instead relying on direct simulation of the far field and all rotor blades. In general, this requires the use of multiblock or overset meshes. Sitaraman et al.[13] and Datta et al.,[14] however, solve only the near field of a single blade and uses fast Biot–Savart evaluation methods to apply induced velocities at all the grid points, where the induced velocities are computed from a free wake model. Pahlke and van der Wall[15] show improved correlation on the 7A and 7AD model rotors in high-speed forward flight with the FLOWer CFD code only when viscous effects are included.

Methodology

CAMRAD II

Structural dynamics and rotor trim for the coupled calculations are performed using the comprehensive rotorcraft analysis CAMRAD II (Ref. 16). In this work, an isolated rotor is modeled as a flexible blade with nonlinear finite elements. The CFD/CSD coupled solutions are compared with state-of-the-art comprehensive analysis-only results. The aerodynamic model in CAMRAD II is based on second-order lifting line theory.[17] The blade section aerodynamic modeling problem in lifting line theory is unsteady, compressible, viscous flow about an infinite wing in a uniform flow consisting of a yawed freestream and wake-induced velocity. This problem is modeled within CAMRAD II as two-dimensional, steady, compressible, viscous flow (airfoil tables), plus corrections for swept and yawed flow, spanwise drag, unsteady loads, and dynamic stall. The wake problem of lifting line theory is an incompressible vortex wake behind the lifting line, with distorted geometry and rollup. The wake analysis calculates the rotor nonuniform induced velocity using a free wake geometry. The tip vortex formation is modeled.

OVERFLOW-D

The CFD calculations use the Reynolds-averaged Navier–Stokes CFD code OVERFLOW-D (Ref. 18). It is based on the OVERFLOW 1.6au code, which has been continually developed at NASA and has been applied to a wide range of fluid dynamics problems. OVERFLOW-D includes major modifications for time-dependent, rigid-body motion of components, in particular individual moving rotor blades that are often required for complex rotorcraft configurations. Previous work has validated the code for aerodynamic performance predictions of rigid-blade helicopter and tiltrotor configurations in hover,[19,20] although wake flowfield details and blade loadings were not grid converged. This work extends the validation to helicopter airloads in edgewise forward flight.

OVERFLOW-D solutions are computed on structured, overset grids using body-conforming near-body grids and automatically generated Cartesian off-body grids.[21] Near-body grids are used to discretize the surface geometries and capture wall-bounded viscous effects. Off-body grids extend to the far field with decreasing grid density and capture the wakes. User-defined subroutines prescribe the arbitrary six-degree-of-freedom motion. The grid motion necessitates recalculation of the domain connectivity, including hole cuts and intergrid boundary point (IGBP) interpolation coefficients, at each time step as the near-body grids move through the stationary off-body grids. Hole cutting, which is required when one grid passes through another, is performed efficiently using the object x-ray technique.[22] Interpolation coefficients are determined using inverse maps and Newton iteration searching. Reuse of information from the preceding time step enables an order of magnitude speed up compared to domain connectivity solutions from scratch. Using this technique, the domain connectivity work can be efficiently performed in less than 20% of the time required for the flow solver.

Because of the aeroelastics of the coupled solutions, several modifications are made to the rigid-body version of OVERFLOW-D. Capability that has been added to account accurately for deforming grids includes implementation of the geometric conservation law, (GCL)[23,24] and freestream preserving, finite volume time metrics[25]; surface grid deformation and volume grid movement; and regeneration of x rays and inverse maps.[26]

Grid Deformation

In addition to rigid-body movement of the rotor blades due to rotor rotation, collective, cyclic, and elastic motion is introduced by the structural mechanics and dynamics. Modifications are made to OVERFLOW-D to allow the blade grids to deform aeroelastically. Given the nature of overset grid generation, it is important that the implementation handle general grid topologies.

First, the surface grids defining the blades are deformed. The motions from CSD are specified as three translations and three rotations of the undeflected blade quarter-chord as a function of radius r/R and azimuth Ψ. These six motions completely contain all of the control inputs, elastics, and dynamics, while also taking into account any geometric quarter-chord variations, for example, tip sweep. All blade deformations are modeled here except for airfoil chord deformations. Any point on the blade surface can be transformed, based its local value of r/R and the current blade azimuth angle, through two-dimensional interpolation of the CSD motions. If C-meshes happen to be used, the points on the wake cut are handled naturally in the same manner. Cubic spline interpolation is employed to maintain C^1 continuity of the motion derivatives, which are related to the grid speeds. Surface point motion is finally computed from a 3×3 transformation matrix that contains both the translational and rotational motions.

Second, the volume grid is adjusted to account for the surface motion. Again, no restrictions are made for particular grid topologies, such as planar grid sections. Field points are moved using the transformation matrix of the associated constant computational coordinate surface point. Through the built-in rotation of the surface point that is transmitted to the field points, grid quality is maintained, including any initial orthogonality.[24] Because IGBP interpolations are recalculated for overset, moving-body problems, there is no savings in specifying that the blade near-body grid outer boundary not move. In fact, any moderate amount of rotor blade flapping requires that the outer boundary deflect in concert with the surface. Outer boundaries of near-body grids are typically only one chord length from the blade surface. The algebraic nature of the calculation makes the cost for high-quality grid deformation relatively low.

X-Ray Regeneration

For static geometries and rigid-body motion, the shape of the hole that the geometry makes with respect to other grids remains fixed, although because of grid motion the hole location is not fixed in time. For deforming geometries neither the hole shape nor location is fixed. When the object x-rays technique is used, deforming surface geometries should be x rayed again to represent the surface accurately, particularly as noted earlier due to flapping. Modifications to OVERFLOW-D integrate the x-ray software GENX as run-time subroutines. X rays are recomputed at a user-defined interval, for example, every 2–5 deg of azimuth. Although the relative cost compared with a flow solver time step is large because the GENX software is not parallelized, recalculation intervals of at least 25 time steps minimize the overall cost.

Parallel Computing

Solutions are computed on large parallel computers or a network of computers communicating with the message passing interface (MPI) protocol. Both the domain connectivity and flow solver modules have been parallelized for efficient, scalable computations using MPI. Coarse grain parallelization on large numbers of processors is achieved by distributing grids among the processors and, if necessary, splitting them as appropriate into smaller blocks to prevent bottlenecks.

Coupling

A loose coupling strategy based on a trimmed, periodic rotor solution is employed. The coupling methodology is an incremental formulation developed previously[7] and outlined in Fig. 1. In summary, in an iterative fashion the methodology completely replaces the comprehensive analysis airloads with CFD airloads, resulting in a consistent, coupled aerodynamic and structural solution.

The coupling calculation is initialized with a comprehensive analysis using lifting line aerodynamics, resulting in a trimmed rotor solution. This run creates initial quarter-chord motions as a function of radius and azimuth, which are transferred to the CFD. The CFD code is run using the specified motions. This initial CFD solution need not be fully converged, and, typically, for a four-bladed rotor in forward flight, $1\text{–}1\frac{1}{4}$ rotor revolutions is sufficient. OVERFLOW-D outputs the surface grid and flow variables at user-specified intervals, typically every 5 deg. It is not necessary or desirable to save the complete flowfield at this interval. The surface files are postprocessed to obtain normal force (NF), pitching moment (PM), and chord force (CF) as a function of radius and azimuth. Only the pressure components of the forces are calculated for the present work. Viscous components of the NF and PM are negligible, and the viscous CF effect is investigated. For completeness and future performance and structural loads predictions, viscous forces should be added to the postprocessing software. NF, PM, and CF are passed to the comprehensive code for the next coupling iteration.

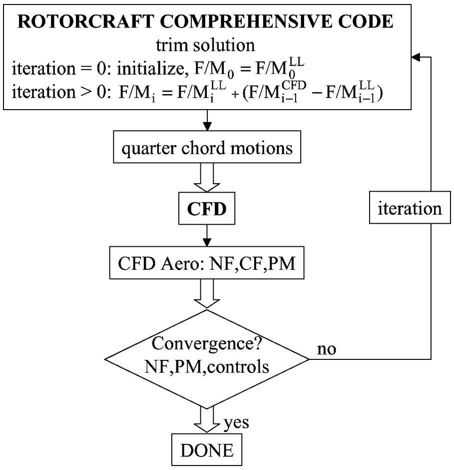

Fig. 1 CFD/CSD loose coupling procedure, *F*/*M* = forces and moments.

Thereafter, the aerodynamic forces and moments F/M that are used in the comprehensive code at the next iteration i are the comprehensive lifting line (LL) solution required to trim, plus a correction based on CFD.

$$F/M_i = F\big/M_i^{\mathrm{LL}} + \left(F\big/M_{i-1}^{\mathrm{CFD}} - F\big/M_{i-1}^{\mathrm{LL}}\right)$$

That is, the correction is the difference between the preceding CFD and comprehensive lifting line solutions. Alternatively, the equation can be written as

$$F/M_i = F\big/M_{i-1}^{\mathrm{CFD}} + \left(F\big/M_i^{\mathrm{LL}} - F\big/M_{i-1}^{\mathrm{LL}}\right)$$

Then it is seen that the forces and moments used in the comprehensive code are those computed by CFD plus an increment required to retrim the rotor. The trim correction should, in general, be small, and all that is required is that the trends of the table lookup be relatively consistent with the CFD. There is a possibility that, while trying to trim, the lifting line aerodynamics will move the solution in the wrong direction. This might be expected when parts of the rotor are stalled. However, for all of the cases demonstrated here, no convergence difficulties were encountered. Currently, it is computationally prohibitive to use CFD inside the trim loop.

With new quarter-chord motions of the retrimmed rotor, the CFD is rerun. Again, it is not necessary to reconverge fully the flow solution, resulting in a form of relaxation. If the preceding CFD calculation is used as a restart condition, for a four-bladed rotor, one-quarter of a revolution is sufficient.

The coupled solution is converged when collective and cyclic control angles and CFD aerodynamic forces do not change between iterations. Plotting accuracy of aerodynamic forces and moments and three significant figures for control angles have been used here. Note that on convergence the total airloads used in the comprehensive code are the CFD airloads. The loose coupling does not retain any aerodynamic terms from lifting line analysis in the final result. This can easily be seen from the preceding equations because at convergence F/M^{LL} does not change between iterations i and $i-1$ because no trim or aeroelastic changes are required. All trim constraints are satisfied by the final CFD solution. If the parameters are not converged, the next coupling iteration begins again with the comprehensive analysis.

Coupling Implementation

The coupling between CAMRAD II and OVERFLOW-D has been integrated with UNIX scripts and FORTRAN postprocessing codes. CAMRAD II and OVERFLOW-D alternately exchange files describing the deflected blade motion and CFD airloads. In practice, the CFD airloads along with the total airloads from the preceding iteration are used to create a delta file. A correction is implemented in the comprehensive analysis as an input increment $\Delta F/M$

$$F/M_i = F\big/M_i^{\mathrm{LL}} + \Delta F/M_i$$

$$\Delta F/M_i = \Delta F/M_{i-1} + \left(F\big/M_{i-1}^{\mathrm{CFD}} - F/M_{i-1}\right)$$

The increment is updated from the difference between the CFD loads and the total comprehensive analysis loads. In this manner, it is not necessary to separate out the lifting line portion.

For efficient, automated coupling, both CAMRAD II and OVERFLOW-D run on the same computer. The cost of the comprehensive solution is, however, at least two orders of magnitude less than the CFD.

UH-60A Configuration and Modeling

Flight-Test Data

A unique and extensive flight-test database exists for a UH-60A helicopter in level flight and transient maneuvers.[27] The data were obtained during the NASA/U.S. Army UH-60A Airloads Program. The database provides aerodynamic pressures, structural loads, control positions, and rotor forces and moments, allowing for the validation of both aerodynamic and structural models. The test matrix contains a range of advance ratios and gross weight coefficients, as shown in Fig. 2, with the test points investigated here indicated. The focus of this paper is on airloads prediction. Absolute pressures

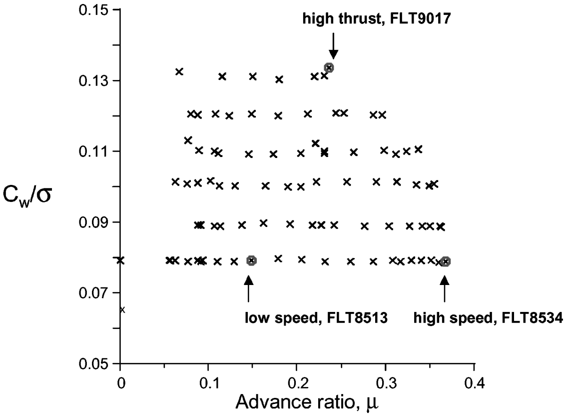

Fig. 2 UH-60A Airloads Program level-flight test matrix.

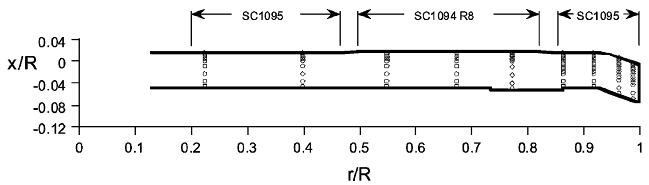

Fig. 3 UH-60A blade planform.

were measured at $r/R = 0.225, 0.40, 0.55, 0.675, 0.775, 0.865, 0.92, 0.965$, and 0.99 (Fig. 3) along the blade chord and integrated to obtain normal force, pitching moment, and chord force.

The data have undergone a significant amount of investigation,[28] however, some discrepancies have not yet been resolved. Measured rotor thrust was determined from the gross weight of the helicopter plus estimates for the fuselage and tail rotor loads. Measured hub moments, roll and pitch, were determined from an upper shaft bending moment gauge. However, integration of the measured pressures over the rotor result in poor agreement with measured thrust and moments. For example, for the high-speed test point, the integrated thrust is 10% higher, and the total integrated hub moment is 50% larger with an 80-deg phase difference compared to the measured values. Consequently, it is clear that there is some uncertainty in the aircraft trim condition, and there will be some discrepancy in comparison of mean airloads values.[29] Errors in the blade pressures can have large effects on integrated section pitching moments. Bad trailing-edge pressure taps have been discovered in this dataset that considerably skew the pitching moment mean values. For this reason, all examples of pitching moment have the mean removed.

An error in UH-60A airloads data postprocessing was discovered in January 2005. The correction has resulted in a negative 14-deg blade azimuth shift in all azimuthally dependent data. The shift is related to a 7-deg difference between the zero azimuth references for flight and analysis. Before 2005, the 7-deg difference in azimuth references had been applied in the opposite direction. All flight-test data in this paper have been corrected.

Comprehensive Modeling

The UH-60A master input database has been used to define the elastic UH-60A 4-bladed rotor model. The database contains geometric, aerodynamic, and structural material properties. Figure 3 shows the blade planform and pressure transducer locations. The blade has a radius of 322 in., SC1095 airfoil chord of 20.76 in., and the swept tip begins at $r/R = 0.929$. The rotor solidity σ is 0.0826, and there is about -16 deg of nonlinear twist. Further details of the blade can be found in Ref. 28.

The comprehensive analysis trim solution for forward flight corresponding to the UH-60A flight-test data solves for the collective and cyclic controls required to obtain the specified (measured) thrust and shaft pitch and roll moments with fixed rotor shaft angle. For the CFD/CSD coupling, all aerodynamics are eventually determined by CFD. Therefore, it is most efficient to use the fastest possible wake model in the comprehensive code, that is, uniform inflow. Additional aerodynamic model features that might alter the input CFD aerodynamics are turned off, such as a tip-loss model.

For comparison of the coupled results with state-of-the-art comprehensive analysis, a multiple trailer consolidation wake model with standard parameters is used.[4] An ONERA EDLIN dynamic stall model[16] is turned on for the high-thrust case. The consolidation model used a constant vortex core radius of 50% chord, chosen based on correlation of calculated and measured airloads for a range of configurations.[4] A 15-deg azimuthal step size is standard for the aerodynamic and structural dynamic calculations in CAMRAD II. This limits the harmonic content of the blade motions to 12/revolution, whereas the aerodynamics contains much higher frequencies.

CFD Modeling

A theoretical UH-60A CFD blade grid was developed using the master database. Definitions of the SC1095 and SC1094R8 airfoils have been combined with twist, chord, quarter-chord location, and trim tab distributions to generate the rotor blade definition. Realistic rounded tip cap and root definitions have also been used. The blunt-trailing-edge airfoils have been closed to a sharp point. Two-dimensional results indicate that this is a reasonable approximation for these airfoils.[30]

Grid generation uses the overset near-body/off-body discretization concept. For each of the four blades, three near-body grids define the blade, root cap, and tip cap. They extend about one chord away from the surface and include sufficient resolution to capture boundary-layer viscous effects. Blade and cap grids use a C-mesh topology. The main blades have dimensions of $249 \times 163 \times 65$ (chordwise, spanwise, and normal). The chordwise leading- and trailing-edge spacings are 0.001 and 0.002 chords, respectively, with 201 points on the airfoil surface. The root and tip cap grids have dimensions $111 \times 59 \times 65$ and $137 \times 59 \times 65$ (chordwise; spanwise, upper and lower surface; and normal), with 87 and 113 streamwise points on the solid surface, respectively. The wake is a C-mesh (foldover) boundary condition in the spanwise direction. The first three points in the normal direction at the blade surface have a constant spacing, calculated to produce a $y^+ \leq 1$. The surface grids on the outboard part of the blade are shown in Fig. 4.

Off-body Cartesian grid generation is automatically performed by OVERFLOW-D. The finest off-body spacing for the baseline grid is 0.10 chords. This level-1 grid surrounds the blades and extends $\pm 1.2R$ in x and y and $\pm 0.3R$ in z. It is manually specified to contain a portion of the wake. Note that a typical wake vortex core size is 0.10 chords, and, therefore, significant dissipation of the wake vortex cores will occur. A total of five progressively coarser levels are generated out to the far-field boundary, which is placed at $5R$ in all directions from the center of the domain. The grid spacings differ by a factor of two between each Cartesian mesh level.

The baseline grid contains 26.1 million points with 55% in the near-body grids. A coarse grid with one-eighth the number of points extracted from the baseline grid is also used in this work. Where grid points of overset meshes fall inside the geometry, hole cutting is employed to blank out these points. A cut through the grid system shown in Fig. 5 shows the deflected near-body grids, level-1 and higher Cartesian off-body grids, hole cuts, and grid overlap. The baseline grid uses double-fringe overlap, whereas the coarse grid uses single fringing. Double fringing allows derivatives as well as flow variables to be smoothly transferred between overlapped grids.

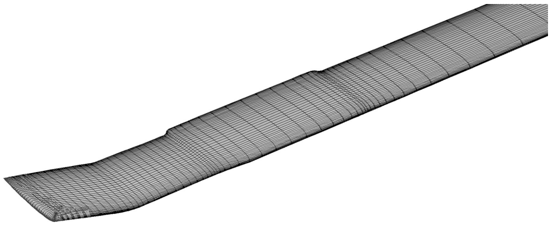

Fig. 4 UH-60A outer blade coarse surface grids.

Table 1 UH-60A flight test counters

Counter	C_T/σ	μ	M_∞	M_{tip}	α_s, deg	β, deg
c8534	0.084	0.37	0.236	0.642	−7.31	1.28
c8513	0.076	0.15	0.096	0.644	0.76	7.71
c9017	0.129	0.24	0.157	0.665	−0.15	−1.58

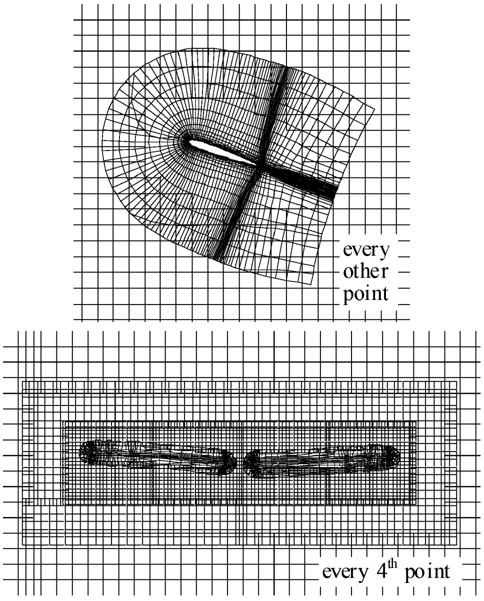

Fig. 5 UH-60A baseline volume grid.

Because of stability limitations, an azimuthal step size of 0.05 deg is used in all CFD calculations, corresponding to 1800 steps per 90 deg of rotation of the four-bladed rotor.

The OVERFLOW-D runs use second-order spatial central differencing with standard second- and fourth-order artificial dissipation and an implicit first-order temporal scheme in the near-body grids. The Baldwin–Barth one-equation turbulence model is employed in the near-body grids, which are assumed fully turbulent. Fourth-order spatial with reduced artificial dissipation, explicit third-order temporal, and inviscid modeling are used in the off-body grids, all to minimize as much as possible any wake diffusion.

Results

Three level-flight UH-60A data points have been used to test the loose coupling procedure and are documented in Table 1. The accuracy, efficiency, and robustness of the CFD/comprehensive coupling procedure will be demonstrated using these test points. Aerodynamics will be investigated through airloads comparisons and flowfield visualization.

High Speed

Flight counter $c8534$ is a high speed, $\mu = 0.37$, level-flight data point. The hover tip Mach number of the UH-60A is approximately 0.64. The freestream Mach number of this point is 0.236. Many investigations have been performed on this flight-test counter to understand unsolved analysis problems of the advancing blade azimuthal phase lag and underprediction of blade pitching moments.[1]

Coupling Convergence

Representative airloads convergence on the baseline grid is shown in Fig. 6. The normal force M^2c_n and pitching moments M^2c_m have converged to plotting accuracy in six iterations. The coupling frequency is 90 deg for the four-bladed rotor. The smooth solutions at 90-, 180-, and 270-deg azimuth indicate this to be an efficient strategy. The advancing side negative loading is the last area to converge. This fast convergence of the loose coupling methodology is in agreement with previous studies.[5,8] Figure 7 shows convergence of the CAMRAD II control angles and trim targets, normalized by their final values. As would be expected, OVERFLOW-D and CAMRAD II airloads converge to the same values.

Table 2 Comparison of converged control angles (degrees) as a function of grid density

Grid	θ_0	θ_{1c}	θ_{1s}	β_0	β_{1c}	β_{1s}
Baseline	14.6	2.39	−8.63	3.43	0.70	2.04
Coarse	14.8	2.44	−8.61	3.43	0.71	2.03

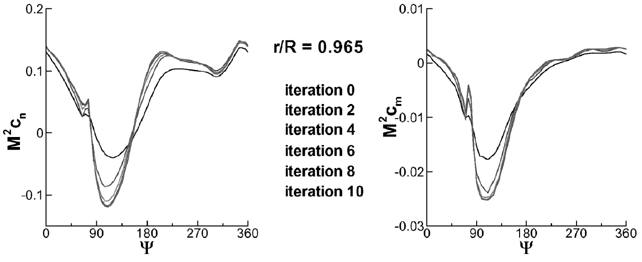

Fig. 6 Airloads convergence, $\mu = 0.37$.

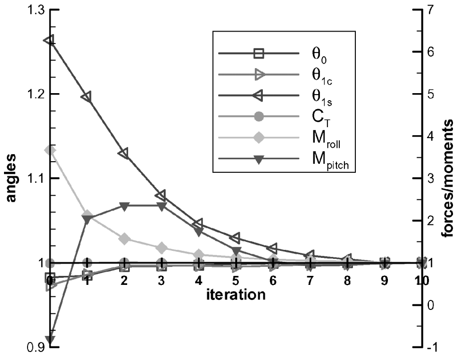

Fig. 7 Trim target and controls convergence, $\mu = 0.37$.

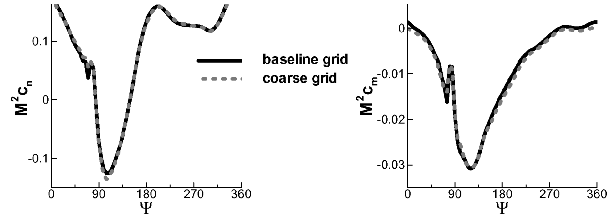

Fig. 8 Grid convergence, $\mu = 0.37$ and $r/R = 0.92$.

Solution Accuracy

A coarse grid, derived by taking every other point from the baseline grid, has been used to investigate grid convergence of the coupled results. Figure 8 shows airloads comparisons at the span station with the largest differences. For this data point, the coarse grid gives almost the same airloads at approximately one-eighth the cost. A comparison of converged control angles for the two coupled solutions is shown in Table 2, indicating good agreement. Coupling convergence histories are similar for the two grid densities as well.

Although the wake is poorly resolved in the coarse grid due to large level-1 off-body spacing, 20% chord, the airloads for this high-speed case are not sensitive to the wake details. The rotor wake is quickly convected past the rotor, which has a relatively large nose down shaft angle. Figure 9 justifies this assertion. A comparison is made between the full, viscous, four-bladed configuration with wake modeling on the coarse grid and a simplified analysis that uses only one isolated, inviscid, coarse grid blade. The wakes from the other blades and the far field are not contained in this one-bladed solution. Both solutions use the same fixed set of quarter-chord motions. It is clear that for the high-speed data point, there is limited wake interaction only in the first quadrant. Similar conclusions are drawn by Pahlke and van der Wall[15] for the 7A model rotor. Most importantly, the wake has no effect on the phase of the advancing side negative loading. These calculations and full-configuration Euler vs Navier–Stokes comparisons also indicate that viscous effects are not important for the UH-60A, unlike results reported by Pahlke and van der Wall, which were quite sensitive to boundary-layer effects.

Variation of the trim target has been investigated to determine solution sensitivity to potential, unknown experimental errors. Neither thrust nor hub moment (phase or magnitude) have a significant effect on the overall character of the airloads.[26] In particular, the phase and magnitude of the advancing side negative loading and wake interactions show only minor changes. Because of the minimal effects, calculations have not been rerun due to the recently discovered 14-deg azimuth reference shift that affects the phase of the measured hub moment trim target.

Because the current coupling postprocessing only includes forces and moments due to pressure, a constant-section drag coefficient, based on two-dimensional CFD airfoil calculations,[30] was added to the calculated chord force. No discernable changes are noted in the airloads other than a small (~1 deg) increase in the lag angle.

The overset grid methodology makes adding a fuselage a straightforward task. A low-fidelity fuselage geometry has been included in the coarse grid calculation. The hub was not included. The primary effect is to induce an upwash on the inboard part of the rotor blade, $r/R < 0.40$, near 180-deg azimuth, thereby increasing the normal force in this region. The change on this part of the rotor affects the overall trim equilibrium and results in a slight redistribution of forces everywhere on the rotor disk. Of note is a significant improvement in pitching moment comparison in the reversed flow region.[26]

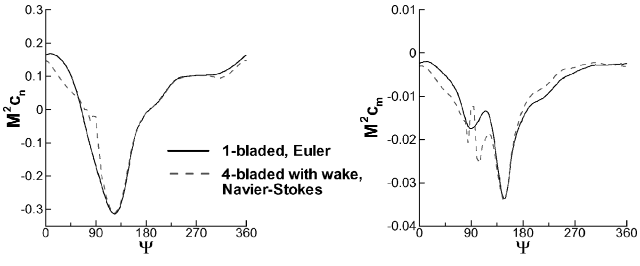

Fig. 9 Viscous and wake effects, $\mu = 0.37$ and $r/R = 0.92$.

Several flow solver parameters were investigated to determine airloads prediction sensitivity. Reduced artificial dissipation and higher-order spatial differencing in the near-body grids and reduced azimuthal step size, $\Delta\psi = 0.025$ deg, all showed no effect on the airloads for the baseline grid. Additionally, results here were not sensitive to the time metric formulation or even satisfaction of the GCL.

Data Comparison

Comparisons of the coupled OVERFLOW/CAMRAD results with flight-test data and CAMRAD II free wake analysis are shown in Fig. 10 for representative span stations. These results are trimmed to the measured thrust and upper shaft bending moments. The magnitudes of the normal force and especially the pitching moment from the coupled solution are in good agreement with the flight-test data. Recall that the mean has been removed from the pitching moment. The shape of the airloads curves are very good. Small discrepancies are seen, such as in the shape of the minimum peak and an inboard impulse around 90-deg azimuth. The shape of the vibratory normal forces, 3/revolution and higher, are in equally good agreement but suffer from a modest underprediction in magnitude. Small, high-frequency oscillations in the test data in the first quadrant resulting from the wake interaction as the blade approaches 90-deg azimuth are beginning to be captured in the coupled solution.

The phase and magnitude of the coupled airloads are significantly improved over the free wake analysis. The underprediction of advancing blade pitching moments and the negative lift phase lag have been remedied. The magnitude of the vibratory forces are also notably improved.

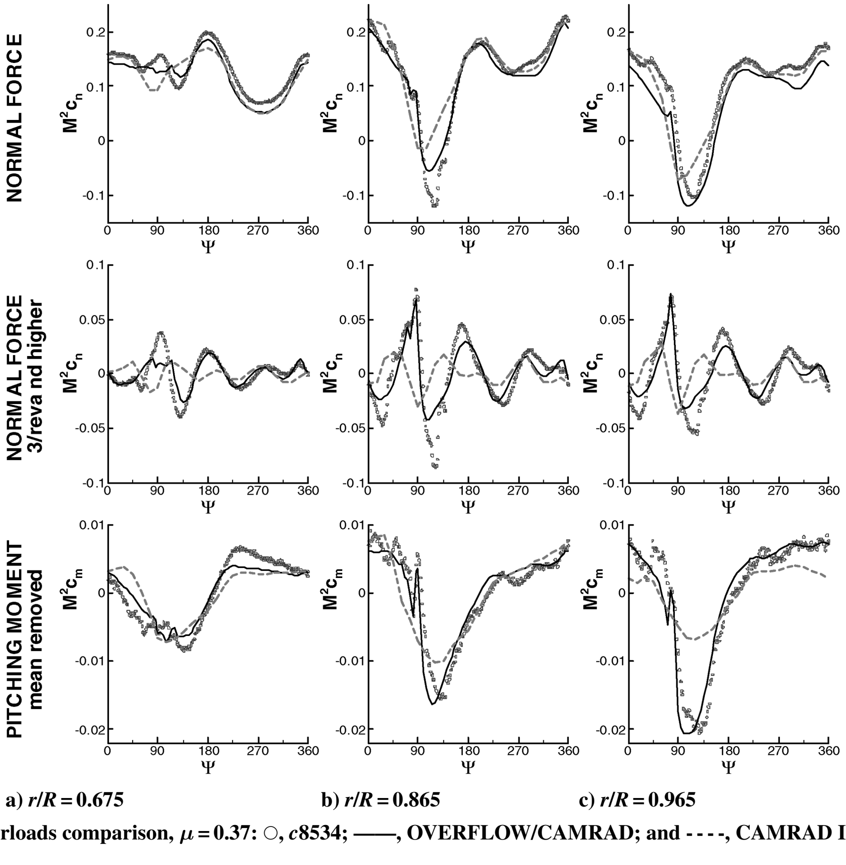

a) $r/R = 0.675$ b) $r/R = 0.865$ c) $r/R = 0.965$

Fig. 10 Airloads comparison, $\mu = 0.37$: ○, c8534; ——, OVERFLOW/CAMRAD; and - - - -, CAMRAD II free wake.

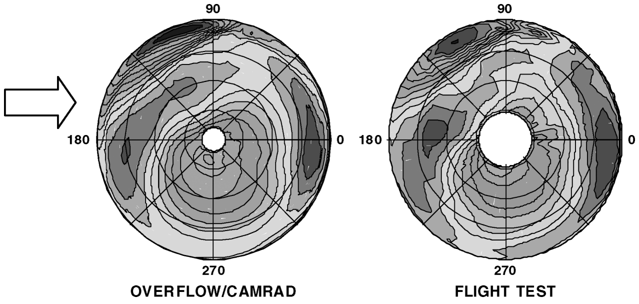

Fig. 11 Rotor disk normal force comparison, $\mu = 0.37$.

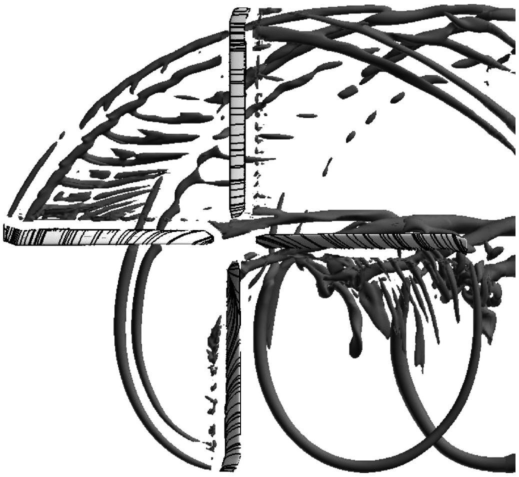

Fig. 12 Wake and surface streamlines, $\mu = 0.37$.

Qualitative comparisons of normal force on the rotor disk are shown in Fig. 11. Note that the overall comparison as well as some of the details are quite good.

Visualization of the wake, shown in Fig. 12, using the Q-criteria,[31] highlights several interesting flow features. Throughout almost the complete azimuth, the blades shed vorticity from the tip and near the sweep break. This indicates the appropriateness of dual-peak or multiple-trailer wake models in comprehensive free wake analyses. A coalescence of vortices around 90-deg azimuth accounts for the airloads oscillations in this region, particularly apparent in pitching moment data. Surface streamline traces (oil flow) on the blades show the swept flow around the azimuth. Reversed flow is seen inboard on the retreating blade; otherwise, there is no separation present.

Low Speed

Flight counter $c8513$ is a low speed, $\mu = 0.15$, level-flight data point. The freestream Mach number of this point is 0.096. At this condition there are significant low-frequency blade–vortex interactions that dominate the airloads. Convergence of the coupling methodology occurs smoothly after nine iterations on the baseline grid. The large sideslip angle, 7.71 deg, was not considered in the comprehensive or CFD calculations; however, in the following comparisons, the flight-test data have been modified to take this into account.

Data Comparison

Comparisons of the coupled OVERFLOW/CAMRAD results with flight-test data and CAMRAD II free wake analysis are shown in Fig. 13 for representative span stations. As with the high-speed test point, the phase and magnitudes of the normal force and pitching moment from the coupled solution are in excellent agreement with the flight-test data. The magnitude and shape of the vibratory normal forces, 3/revolution and higher, also show good agreement between the test data and analysis. Some of the details in the comparisons, such as minor oscillations and overshoots, are quite remarkable.

The blade–vortex interaction normal force impulses at 90- and 270-deg azimuth are captured accurately and sharply. At $r/R = 0.675$, the blade–vortex interaction is underpredicted in the second quadrant.

Although the free wake analysis is acceptable for this flight condition, the coupled solution still shows an improvement in the shape of the curves, particularly in the second quadrant. The pitching moments are somewhat improved. Unlike the free wake analysis, the coupled analysis begins to capture the pitching moment impulse at $r/R = 0.965$ and $\psi = 270$ deg, but both are smeared out at $r/R = 0.865$.

Qualitative comparisons of normal force (mean removed) on the rotor disk are shown in Fig. 14. The overall comparison is excellent. In both Fig. 14a and 14b, the strong blade–vortex interaction impulses outboard on the advancing and retreating blades are well defined.

Comparisons of the coupled, free wake, and experimental mean normal force distributions are shown in Fig. 15. Clearly, the coupled and free wake solutions trimmed to the measured thrust, $C_T/\sigma = 0.076$, are not generating the same thrust as the integrated airloads, $C_T/\sigma = 0.087$. The CAMRAD II free wake analysis matches the outboard, swept tip loading much better, but this implies even larger disagreement with the inboard test data. When this mean discrepancy is removed from the normal force airloads comparisons, the agreement between test and coupled analysis is even more noteworthy (Figs. 13 and 14).

Wake Visualization

Visualization of the wake shown in Fig. 16 shows multiple blade–wake interactions. Wake structures in the second and third quadrants can be matched up with the normal force distributions in Fig. 14. Inaccurate correlation with the blade–vortex interaction near $r/R = 0.65$ and $\psi = 120$ deg in the test data, however, indicates that some wake structures may not be correctly captured. Several tip vortices from the different blades are visible, but generally more than one revolution cannot be maintained in the off-body grids. The roll up of the wake vortices into the supervortices are more evident than in the high-speed calculation.

Grid Effects

Surprisingly, there are no airloads differences seen in the coarse grid results other than a slight reduction in the peaks of the impulses from the blade–vortex interactions.[26] It was somewhat unexpected that either grid, with wake grid spacings on the order of a physical tip vortex core, would have been able to resolve so accurately the wake interactions with the blades. An even finer off-body grid was generated with level-1 spacing of 0.05 chords, in conjunction with the baseline near-body grid system. The total number of grid points is 98 million. Results from that calculation using the coupled, baseline grid motions still show no significant effects due to wake resolution. Although the comprehensive free wake analysis results for the UH-60A low-speed flight condition are highly dependent on the wake model and core size used,[4] the CFD, on the other hand, seems insensitive to attempts to improve the solutions through reduced numerical viscosity or grid refinement. This is probably a result of the fact that the actual vortex cores are not resolved.

High Thrust

Flight counter $c9017$ is an intermediate speed, $\mu = 0.24$, high-thrust-coefficient, level-flight test point flown at 17,000 ft. The freestream Mach number is 0.157, and the hover tip Mach number has increased to 0.665. This is a challenging and quintessential rotorcraft test case due to the wide variation of unsteady flow conditions, ranging from transonic to stall, with noticeable wake interactions. The dynamic stall characteristics of this test point have previously been discussed in detail.[32]

Convergence of the coupling methodology occurs after 10 iterations on the baseline grid. One might suspect that if any conditions would have coupling convergence difficulties it would be a case with highly unsteady phenomena such as dynamic stall. The coupling convergence history, however, is well behaved, and no changes in coupling strategy or frequency are required.

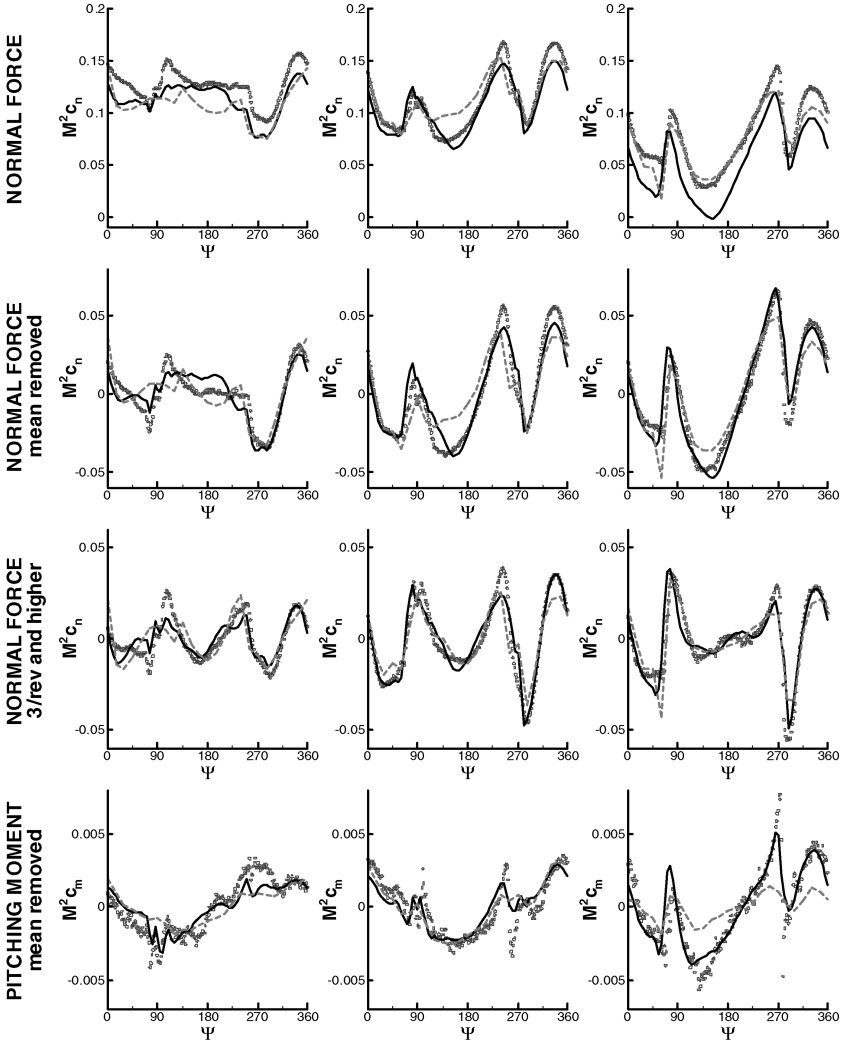

a) $r/R = 0.675$ **b)** $r/R = 0.865$ **c)** $r/R = 0.965$

Fig. 13 Airloads comparison, $\mu = 0.15$: ○, c8513; ——, OVERFLOW/CAMRAD; and - - - -, CAMRAD II free wake.

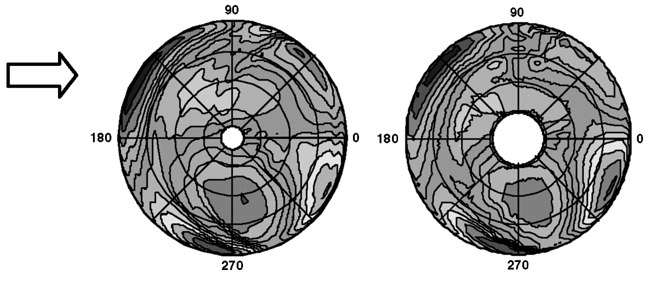

a) OVERFLOW/CAMRAD **b) Flight test**

Fig. 14 Rotor disk normal force (mean removed) comparison, $\mu = 0.15$.

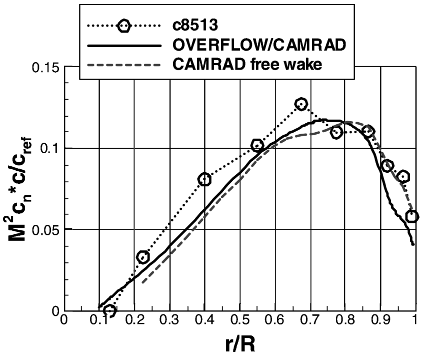

Fig. 15 Mean normal force distribution, μ = 0.15.

Data Comparison

Comparisons of the coupled OVERFLOW/CAMRAD results and CAMRAD II free wake analysis with flight-test data are shown in Fig. 17 for representative span stations. Overall, the agreement between flight-test and coupled results is respectable, although not as good as the preceding cases. The phase, magnitude, and shape of the pitching moments curves are in particularly good agreement with the test data.

The major discrepancies between the flight-test and the OVERFLOW/CAMRAD coupled solution are in normal force prediction on the outboard part of the blade. On the advancing side there is considerable disagreement in the steepness with which the minimum peak loading region is entered and departed. The normal force distributions also lack the higher level and overshoot oscillations in the third quadrant from 220- to 270-deg azimuth. In comparison, the comprehensive free wake analysis somewhat captures the overshoot oscillations at the end of the third quadrant. Based on the wake visualization, this overshoot and oscillation could be a blade–vortex interaction that is poorly captured.[26]

The dynamic stall encounters, evidenced by the large negative pitching moments, are initiated at the correct location. The extent of the calculated stall regions generally correspond to the flight-test regions, with some underprediction of the spanwise extent at $r/R = 0.775$ (not shown) and 0.965. However, the flight-test data shown are only the first revolution, and other revolutions indicate varying extent of the unsteady, nonperiodic stall. The pitching moments in the stalled region show good oscillatory magnitude for prediction of pitch link loads at this level-flight test point.

Qualitative comparisons of normal force and pitching moment on the rotor disk from the OVERFLOW/CAMRAD coupled analysis and flight test are shown in Fig. 18. The comparison is generally good. As first indicated by the line plots, pitching moment is in especially good agreement, with all major features duplicated in the analysis. Normal force comparisons in the first quadrant are poor. The second quadrant indicates a computed minimum peak loading region that is larger in extent azimuthally but smaller radially.

Stall Regions

Several criteria can be used to detect separation or stall: section normal force break, section pitching moment break, trailing-edge pressure divergence, surface streamlines, and chordwise skin friction. In Fig. 18, regions of stall on the rotor disk are apparent in the pitching moment and normal force as abrupt reductions in these quantities (dark). The progression is from midspan to outboard for the first dynamic stall cycle. The second stall cycle is confined to the outboard section, $r/R > 0.75$. The normal force and pitching moment are consistent in their predictions.

A dynamic stall rotor map is created using the various stall detection criteria, as shown in Fig. 19. All criteria are somewhat subjective. Stall initiation lines based on normal force and pitching moment gradients are indicated. Regions of separation based on 96% chord upper surface pressure coefficient divergence of −0.06

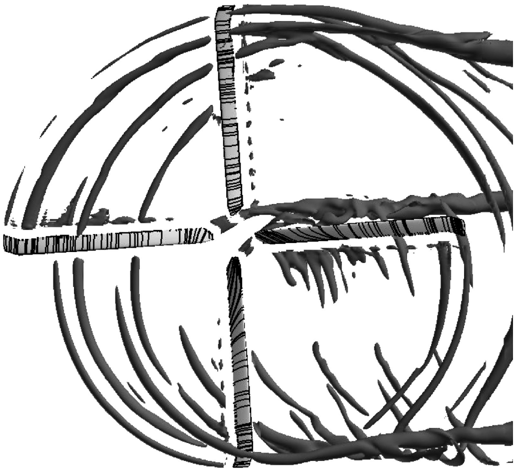

Fig. 16 Wake and surface streamlines, μ = 0.15.

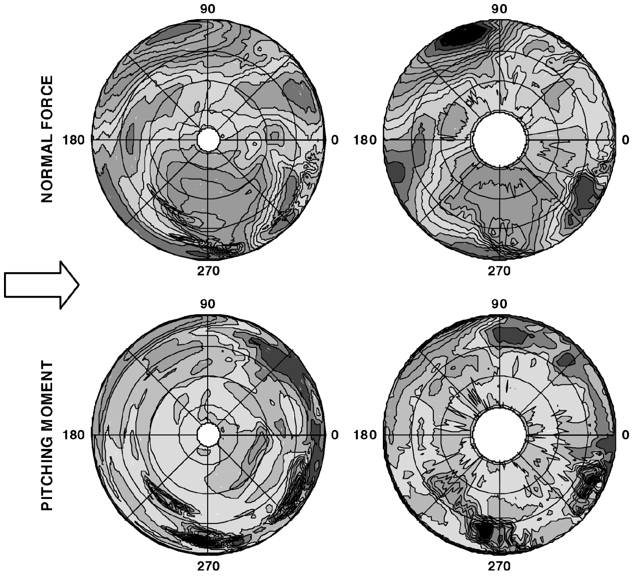

a) OVERFLOW/CAMRAD **b) Flight test**

Fig. 18 Rotor disk airloads comparison (mean removed), μ = 0.24 and high C_T.

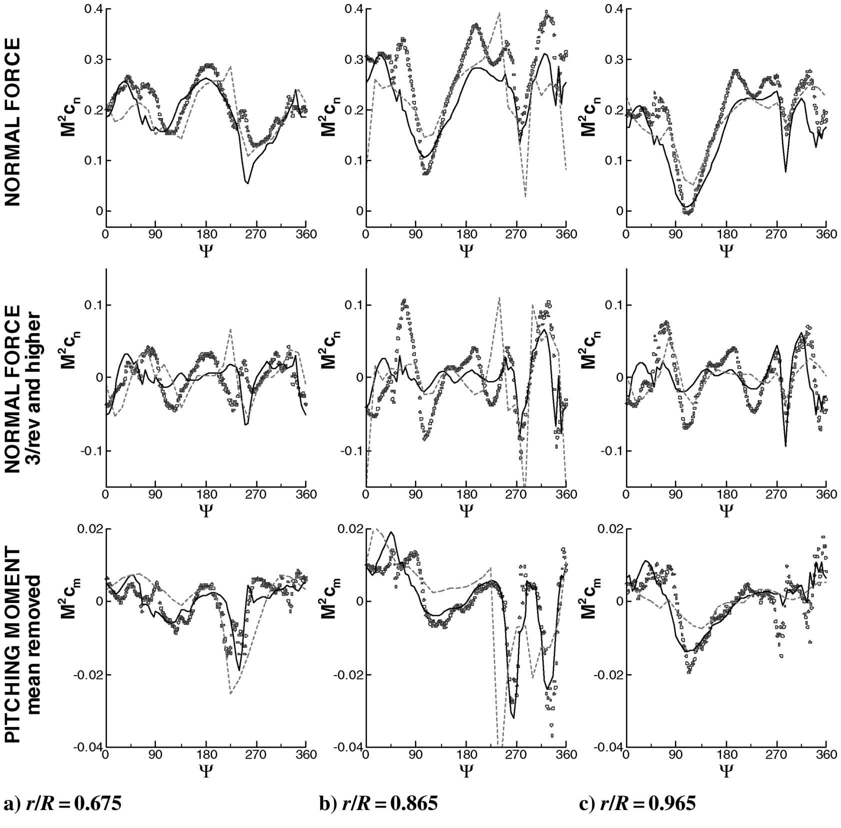

a) $r/R = 0.675$ **b) $r/R = 0.865$** **c) $r/R = 0.965$**

Fig. 17 Airloads comparison, $\mu = 0.24$ and high C_T: ○, $c9017$; ——, OVERFLOW/CAMRAD; and - - - -, CAMRAD II free wake.

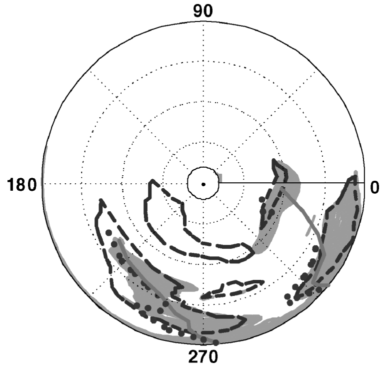

a) OVERFLOW/CAMRAD

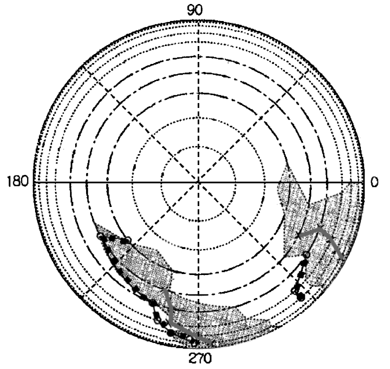

b) Flight test[32]

Fig. 19 Comparison of dynamic stall rotor maps, $\mu = 0.24$ and high C_T: ——, lift stall; ●●●●●●, moment stall; shading, upper surface pressure coefficient $x/c = 0.96$; and zero skin friction, – – –.

from the mean are shaded. Regions of zero chordwise skin friction at $x/c = 0.96$ are also indicated for the coupled solution. There is general agreement among all of the stall/separation criteria. The skin-friction criteria also identifies some of the reversed flow region.

The stall rotor map developed from the CFD solution is compared with that from flight test (Ref. 32, corrected). The dynamic stall regions are in remarkable agreement. The only discrepancy is the inboard extent of the second cycle and the disconnect between the two CFD regions there. It seems there is only mild stall inboard of $r/R = 0.75$, based on inconsistencies between the normal force, pitching moment, and pressure coefficient criteria in both analysis and flight test. Near 180-deg azimuth, a separation region can be identified by the zero chordwise skin-friction and surface streamlines. Note that the flight-test stall rotor maps for higher load factor maneuvers (pull up or diving turn) show that the dynamic stall next occurs in this region. The CFD calculation already hints at a tendency for the flow to separate there.[32]

Grid Effects

The high-thrust, dynamic stall test point does show some sensitivity to grid density.[26] In general, the coarse grid shows earlier separation inboard on the retreating blade than the baseline grid by approximately 15 deg. Outboard, the coarse grid moment stall extent is increased. This indicates that the phase of the stall cycles on the retreating side of the rotor is sensitive to computational modeling details. Changes in the stall location on the retreating side and resulting retrim do not significantly affect the advancing side airloads.

Note that further validation is required for this flight condition because CFD is notoriously fickle in predicting stall. Even though two-dimensional CFD has shown good correlation in predicting static stall for the UH-60 SC1095 airfoil,[30] two- and three-dimensional dynamic stall predictions are an area of ongoing research for which CFD has not yet been validated. A more accurate and advanced turbulence model than the Baldwin–Barth model should be investigated. For overall stall prediction, however, the coupled, turbulent Navier–Stokes results are an improvement over table lookup with dynamic stall modeling.

Computational Cost

All solutions were run on an IBM pSeries 690 parallel supercomputer with 1.4-GHz Power4 processors. The baseline grid was run on 80 processors and required 4.7 h per coupling iteration (90 deg of revolution). The coarse grid, however, requires only 16 processors and 2.0 h per coupling iteration. Therefore, a converged, coupled, coarse grid solution for airloads prediction can be obtained from scratch in approximately 20–28 wallclock hours, or 12–20 h if flow-solver restart capability is used at the start of the coupling. Although still too expensive for design work, coupled CFD and comprehensive analysis of forward-flight rotor configurations is quickly approaching the point where a reasonable matrix of test points could be run on desktop processors.

Conclusions

A Navier–Stokes CFD code OVERFLOW-D has been loosely coupled on a per revolution, periodic basis with a rotorcraft comprehensive code CAMRAD II. The CFD models the complete helicopter configuration using turbulent, viscous flow, and a first-principles-based wake. CFD aerodynamics (normal force, pitching moment, and chord force) are applied in the comprehensive code using an incremental, iterative methodology for trim and aeroelastics. A complete range of level flight conditions has been demonstrated: high speed with advancing blade negative lift, low speed with blade–vortex interactions, and high thrust with dynamic stall. Airloads have been compared with data from the UH-60A Airloads Program and state-of-the-art comprehensive free wake analysis. Wake visualizations and rotor stall maps were extracted from the CFD solutions to show flowfield details. The following conclusions are made from the results presented:

1) Loose coupling is efficient and robust for a wide range of helicopter flight conditions. All of the force and moment components (normal force, pitching moment, and chord force) can be coupled without convergence problems.

2) CFD/comprehensive coupled analysis can be a significant improvement over comprehensive lifting line aerodynamics with free wake and dynamic stall models. Normal force and pitching moment magnitudes are accurately captured in the coupled solutions. The shape of the airloads curves is usually quite accurate.

3) The phase of the airloads in coupled solutions when compared with test data is very good for all flight conditions. The coupled solutions resolve past problems of airloads phase prediction using comprehensive analysis.

4) Unknown, systematic differences between measured and integrated thrust and hub moments in the UH-60A airloads measurements make comparison of mean values and trim conditions problematic, although this is no different than many other experimental databases.

Overall, this work shows that CFD/comprehensive code coupling is fast becoming an attainable and accurate tool for the rotorcraft analyst. In addition, the CFD solutions provide a wealth of aerodynamic information that can be investigated for detailed flow phenomenon.

Acknowledgment

The computer resources of the Department of Defense Major Shared Resource Centers are gratefully acknowledged.

References

[1] Bousman, W. G., "Putting the Aero Back into Aeroelasticity," *8th Army Research Office Workshop on Aeroelasticity of Rotorcraft Systems*, Oct. 1999; NASA TM 2000-209589, March 2000.

[2] Nguyen, K., and Johnson, W., "Evaluation of Dynamic Stall Models with Flight Test Data," *54th Annual Forum*, American Helicopter Society, Alexandria, VA, May 1998.

[3] Lim, J. W., and Anastassiades, T., "Correlation of 2GCHAS Analysis with Experimental Data," *Journal of the American Helicopter Society*, Vol. 40, No. 4, 1995, pp. 18–33.

[4] Yeo, H., and Johnson, W., “Assessment of Comprehensive Analysis Calculation of Airloads on Helicopter Rotors,” *Journal of Aircraft*, Vol. 42, No. 5, 2005, pp. 1218–1228.

[5] Altmikus, A. R. M., Wagner, S., Beaumier, P., and Servera, G., “A Comparison: Weak versus Strong Modular Coupling for Trimmed Aeroelastic Rotor Simulations,” *58th Annual Forum*, American Helicopter Society, Alexandria, VA, June 2002.

[6] Pomin, H., and Wagner, S., “Aeroelastic Analysis of Helicopter Blades on Deformable Chimera Grids,” *Journal of Aircraft*, Vol. 41, No. 3, 2004, pp. 577–584.

[7] Tung, C., Caradonna, F. X., and Johnson, W., “The Prediction of Transonic Flows on an Advancing Rotors,” *Journal of the American Helicopter Society*, Vol. 31, No. 3, 1986, pp. 4–9.

[8] Kim, K.-C., Desopper, A., and Chopra, I., “Blade Response Calculations Using Three-Dimensional Aerodynamic Modeling,” *Journal of the American Helicopter Society*, Vol. 36, No. 1, 1991, pp. 68–77.

[9] Strawn, R. C., Desopper, A., Miller, M., and Jones, A., “Correlation of PUMA Airloads—Evaluation of CFD Prediction Methods,” Paper 14, *15th European Rotorcraft Forum*, Sept. 1989.

[10] Strawn, R. C., and Bridgeman, J. O., “An Improved Three-Dimensional Aerodynamics Model for Helicopter Airloads Prediction,” AIAA Paper 91-0767, Jan. 1991.

[11] Beaumier, P., “A Coupling Procedure Between a Rotor Dynamics Code and a 3D Unsteady Full Potential Code,” *3rd Decennial Specialists’ Conference on Aeromechanics*, American Helicopter Society, Alexandria, VA, Jan. 1994.

[12] Servera, G., Beaumier, P., and Costes, M., “A Weak Coupling Method Between the Dynamics Code HOST and the 3D Unsteady Euler Code WAVES,” *Aerospace Science and Technology*, Vol. 5, No. 6, 2001, pp. 397–408.

[13] Sitaraman, J., Datta, A., Baeder, J. D., and Chopra, I., “Fundamental Understanding and Prediction of Rotor Vibratory Loads in High-Speed Forward Flight,” *29th European Rotorcraft Forum*, Sept. 2003.

[14] Datta, A., Sitaraman, J., Baeder, J., and Chopra, I., “Analysis Refinements for Prediction of Rotor Vibratory Loads in High-Speed Forward Flight,” *60th Annual Forum*, American Helicopter Society, Alexandria, VA, June 2004.

[15] Pahlke, K., and van der Wall, B., “Calculation of Multibladed Rotors in High-Speed Forward Flight with Weak Fluid-Structure-Coupling,” *27th European Rotorcraft Forum*, Sept. 2001.

[16] Johnson, W., “Rotorcraft Aerodynamic Models for a Comprehensive Analysis,” *54th Annual Forum*, American Helicopter Society, Alexandria, VA, May 1998.

[17] Johnson, W., “Recent Developments in Rotary-Wing Aerodynamic Theory,” *AIAA Journal*, Vol. 24, No. 8, 1986, pp. 1219–1244.

[18] Chan, W. M., Meakin, R. L., and Potsdam, M. A., “CHSSI Software for Geometrically Complex Unsteady Aerodynamic Applications,” AIAA Paper 2001-0593, Jan. 2001.

[19] Strawn, R. C., and Djomehri, M. J., “Computational Modeling of Hovering Rotor and Wake Aerodynamics,” American Helicopter Society, May 2001.

[20] Potsdam, M. A., and Strawn, R. C., “CFD Simulations of Tiltrotor Configurations in Hover,” American Helicopter Society, June 2002.

[21] Meakin, R. L., “Automatic Off-Body Grid Generation for Domains of Arbitrary Size,” AIAA Paper 2001-2536, June 2001.

[22] Meakin, R. L., “Object X-Rays for Cutting Holes in Composite Overset Structured Grids,” AIAA Paper 2001-2537, June 2001.

[23] Thomas, P. D., and Lombard, C. K., “Geometric Conservation Law and Its Application to Flow Computations on Moving Grids,” *AIAA Journal*, Vol. 17, No. 10, 1979, pp. 1030–1037.

[24] Morton, S. A., Melville, R. B., and Visbal, M. R., “Accuracy and Coupling Issues of Aeroelastic Navier–Stokes Solutions on Deforming Meshes,” *Journal of Aircraft*, Vol. 35, No. 5, 1998, pp. 798–805.

[25] Obayashi, S., “Freestream Capturing for Moving Coordinates in Three Dimensions,” *AIAA Journal*, Vol. 30, No. 4, 1992, pp. 1125–1128.

[26] Potsdam, M. A., Yeo, H., and Johnson, W., “Rotor Airloads Prediction Using Loose Aerodynamic/Structural Coupling,” *60th Annual Forum*, American Helicopter Society, Alexandria, VA, June 2004.

[27] Kufeld, R. M., Balough, D. L., Cross, J. L., Studebaker, K. F., Jennison, C. D., and Bousman, W. G., “Flight Testing of the UH-60A Airloads Aircraft,” *50th Annual Forum*, American Helicopter Society, Alexandria, VA, May 1994.

[28] Bousman, W. G., and Kufeld, R. M., “UH-60A Airloads Catalog,” NASA TM 2005-212827, Aug. 2005.

[29] Ormiston, R. A., “An Investigation of the Mechanical Airloads Problem for Evaluating Rotor Blade Structural Dynamics Analysis,” *4th Decennial Specialists’ Conference on Aeromechanics*, American Helicopter Society, Alexandria, VA, Jan. 2004.

[30] Smith, M. J., Wong, T. C., Potsdam, M. A., Baeder, J., and Phanse, S., “Evaluation of Computational Fluid Dynamics to Determine Two-Dimensional Airfoil Characteristics for Rotorcraft Applications,” *Journal of the American Helicopter Society*, Vol. 51, No. 1, 2006, pp. 70–79.

[31] Jeong, J., and Hussain, F., “On the Identification of a Vortex,” *Journal of Fluid Mechanics*, Vol. 285, 1985, pp. 69–94.

[32] Bousman, W. G., “A Qualitative Examination of Dynamic Stall from Flight Test Data,” *Journal of the American Helicopter Society*, Vol. 43, No. 4, 1998, pp. 279–295.